water

MDPI

Article

Quantitative 3D Characterization of Pore Structure in Malan Loess from Different Regions of the Loess Plateau

Yalin Nan [1], Ya-Ni Wei [2,*], Kui Liu [1] and Yanbo Cao [2]

[1] China DK Comprehensive Investigate and Design Research Institute Co., Ltd., Xi'an 710054, China; nan.yalin@dky53.com (Y.N.); kyfz@dky53.com (K.L.)
[2] College of Geology Engineering and Geomatics, Chang'an University, Xi'an 710054, China; caoyanbo@chd.edu.cn
* Correspondence: weiyani2006@126.com

Abstract: The micro pores in loess show regional variation in structure on the Loess Plateau and greatly influence the physical properties and macro behaviors of loess. In this study, the 3D microstructures of Malan loess from Lanzhou (LZ), Qingyang (QY), Hengshan (HS) and Jingyang (JY) were established based on μ-CT scanning, and the corresponding microstructural parameters were compared and analyzed quantitatively. The results indicate that the LZ and HS loess both show overall homogeneous structures with dominant inter-particle pores, while the QY and JY loess have more intra-aggregate and constricted pores. Overall, the LZ loess has the largest pore size, followed by the JY loess, QY loess and HS loess, which is consistent with the throat sizes of the four loess samples. The average coordination numbers (CNs) of the LZ and HS loess are lower than those of the QY and JY loess, while the throat lengths of the former two loess are larger than those of the latter two loess. Analysis of the correlation between the micropore parameters and macro behaviors of the loess suggests that the void ratio is the precondition for loess collapse, but it shows weak relevance to collapsibility; meanwhile, the size of pores contributing to the major pore space presents a strong positive correlation. The throat length representing the pore structure is more closely related to loess permeability compared with the void ratio, average CN and throat size.

Keywords: collapsibility; Malan loess; permeability; pore structure; pore throat

check for updates

Citation: Nan, Y.; Wei, Y.-N.; Liu, K.; Cao, Y. Quantitative 3D Characterization of Pore Structure in Malan Loess from Different Regions of the Loess Plateau. *Water* **2023**, *15*, 3151. https://doi.org/10.3390/w15173151

Academic Editor: Chris Bradley

Received: 26 June 2023
Revised: 25 August 2023
Accepted: 30 August 2023
Published: 3 September 2023

1. Introduction

The Loess Plateau, located in the northwest of China, is famous worldwide for its loess distribution, with a wide range and large thickness [1,2]. The Loess Plateau witnesses a great number of geological hazards every year due to the intrinsic properties of loess such as water sensitivity and collapsibility [3,4], especially with the increasing number of extreme weather events. For example, the extreme rainfall in the northern part of Shaanxi Province in 2013 caused more than 8000 disasters [5]. The rainstorm in Zhengzhou city in 2021 induced serious urban flooding and countless landslides and falls. It is generally believed that the special microstructure within loess primarily contributes to its water sensitivity and macro mechanical behaviors [6–10]. As a loose aeolian sediment in the Quaternary, loess is a typical structural soil, forming in the process of accumulation and pedogenesis. The microstructure of loess refers to the size, shape and orientation of particles and pores as well as bonding materials and forms [11,12]. Influenced by source materials, transport distances, sedimentary environment, topography and geomorphology, the particles within loess show various morphologies, size distributions, packing types and bonding forms in different loess regions, which determines the complexity of and variation in the pore structure of the Loess Plateau [6,12,13].

Micro pores within loess are an important microstructural parameter because they greatly influence the physical properties and macro behaviors of loess. For example, the pore size distribution (PSD) and connectivity are closely linked to the permeability and water retention of loess [9,14–17]. Xu et al. established a relationship between the saturated permeability of remolded loess and dry density [9]. Li et al. attributed the soil-water characteristic of loess from different regions to their PSDs [17]. Most studies agree that collapse is actually a transformation from loose particles packing with large pores to denser ones with small pores. The pores provide considerable space for macro collapse deformation [7,18–20]. At present, it is universally acknowledged that micropores in loess can be primarily divided into three types: spaced pores with a larger size than the surrounding particles; inter-particle (aggregate) pores with relatively free channels; and intra-aggregate pores within clay aggregates [21–23]. The first two types both belong to the pores among skeleton particles or clay aggregates. Early research focused on the classification of loess microstructures considering particle packing and bonding as well as pore size and indicated that spaced and inter-particle structures with weak cementations, forming spaced and inter-particle (aggregate) pores, are widely observed in the northwest of the Loess Plateau, while coagulum structures, forming a large amount of intra-aggregate pores, predominate in the southeast [22].

Mercury intrusion porosimetry (MIP) and scanning electron microscopy (SEM) have been widely used to characterize micropores within loess since the 1980s. The MIP method can determine the PSD over a wide range in 3D space, while other related parameters cannot be obtained [24]. SEM is generally used to characterize pore structures in a 2D plane. Recently, computed tomography (CT) and even micro-CT (µ-CT) with a high resolution have been increasingly adopted to characterize pore structure non-destructively [25–27]. Combined with image processing, the 3D morphology of pores can be visualized, and the microstructural parameters such as the pore size, shape, orientation and connectivity can be quantitatively characterized directly in a 3D space, which is believed to be more objective when describing pore structure [13,19,25]. Some scholars investigated 3D microstructure changes in response to loading and wetting based on µ-CT technology to explore the intrinsic mechanisms of macro behaviors [19,28,29], and others even designed an apparatus that can be used to conduct collapse tests on loess samples of several millimeters to capture the loess microstructure evolution within a same sample using µ-CT technology [20].

At present, research on the pore structure within loess or its evolution in a 3D space primarily focuses on a specific region of the Loess Plateau. As described above, micropores in loess are extremely complex and vary in different regions. It is therefore necessary to establish the 3D pore structure of loess from different regions and conduct a statistical analysis and comparison of related pore parameters, which can help to better interpret the physical properties and macro behaviors of loess, such as its water retention, collapsibility and permeability. In this study, Malan loess from different regions of the Loess Plateau were collected to establish their 3D microstructures based on µ-CT scanning. The parameters related to micropores were analyzed and compared quantitatively, and their influences on loess permeability and collapsibility were investigated to interpret the intrinsic mechanisms of the macro behaviors.

2. Materials and Methods

2.1. Soil Sampling and Description

Early research divided the Loess Plateau into three zones, namely the sandy loess zone, silty loess zone and clayey loess zone, according to the particle size distribution [30], as shown in Figure 1. Therefore, four groups of Malan loess from Lanzhou city (silty loess zone), Qingyang city (silty loess zone), Hengshan county (sandy loess zone) and Jingyang county (clayey loess zone), China, named LZ loess, QY loess, HS loess and JY loess, respectively, were selected as the studied loess (Figure 1). All the loess samples were collected at a depth of 3–4 m from natural loess hills, cut into approximate cubes measuring 20 cm on each side and then immediately wrapped in multiple layers of plastic film and placed into an iron sheet box to reduce disturbance during transportation and variations in the water content.

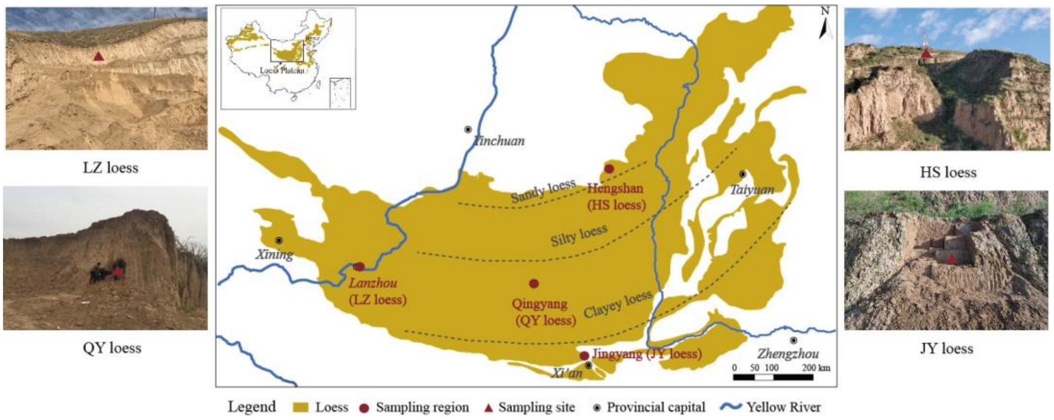

Figure 1. Sampling sites on the Loess Plateau.

The physical parameters of the loess samples were determined by referring to the Specification of Soil Tests and are summarized in Table 1 [31]. Compared with the QY and HS loess, the LZ and JY loess have a more porous structure with a void ratio larger than 1. The particle size distributions that were measured using a laser particle analyzer (Figure 2) show that silt particles (2–75 μm) predominate in all loess samples, accounting for 77–91%. Overall, the soil particles within the HS and LZ loess from the north and northwest areas of the Loess Plateau are coarser than those within the QY and JY loess from the central and southeast areas. In particular, the sand particle (>75 μm) content in the HS loess is much higher than that of the other three loess samples, while its clay particle (<2 μm) content is lower.

Table 1. Physical parameters of the loess samples.

Samples	Density (g/cm^3)	Water Content (%)	Void Ratio	Liquid Limit (%)	Plastic Limit (%)
LZ	1.36	7.2	1.14	24	16
QY	1.59	13.5	0.93	31	18
HS	1.63	7.6	0.79	25	16
JY	1.36	11.0	1.21	33	19

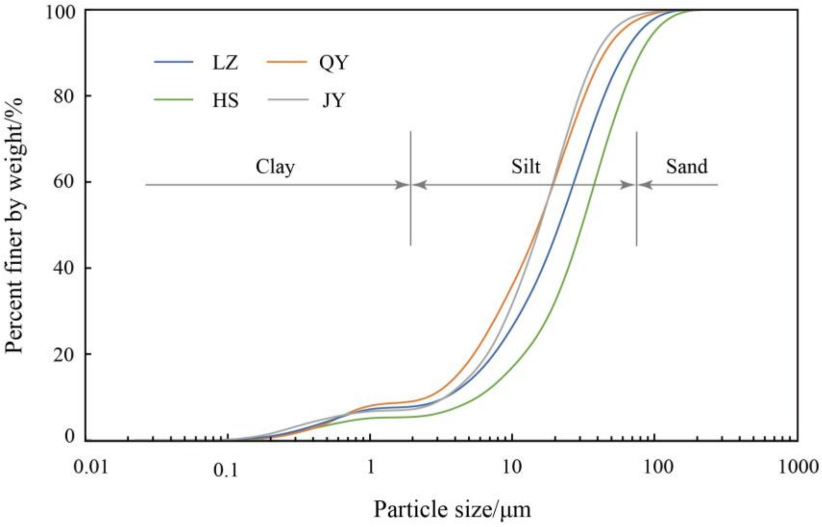

Figure 2. Particle size distributions of the studied loess.

In the four loess samples, quartz, plagioclase and calcite are the main non-clay minerals, with total percentages ranging from 68% to 76%, as presented in Table 2; the clay mineral contents in the four loess samples vary from 16% to 21%.

Table 2. Mineral components in the loess samples.

Samples	Quartz	Potash Feldspar	Plagioclase	Calcite	Amphibole	Dolomite	Clay Mineral
LZ	40%	6%	13%	15%	6%	2%	18%
QY	42%	7%	15%	11%	4%	--	21%
HS	48%	5%	18%	10%	3%	--	16%
JY	46%	4%	15%	12%	3%	--	20%

2.2. Microstructure Observation and Image Processing

2.2.1. Micro-Computed Tomography Scanning

The loess samples from the four sampling sites were air-dried and carefully cut into cylinders approximately 2 mm in diameter and 5 mm in height before being placed into a straw with a similar diameter to avoid shaking in the process of scanning. To avoid the influence of visible fissures on the homogeneity of the loess, three cylindrical samples from each sampling site were produced and scanned using CT with a low resolution of tens of microns to exclude samples with visible fissures. Residual samples with an overall homogeneous structure then underwent a high-resolution scanning at a microscale. Therefore, the samples used for CT scanning well represented the microstructure in loess. The scanning work was conducted using an Xradia 520 Versa 3D X-ray microscope developed by the Zeiss company in Oberkochen, Germany, with a spatial resolution of 1 μm. The scanning range was 1 mm both in diameter and height. After scanning, 1000 CT images were obtained for each sample.

2.2.2. Establishment of 3D Microstructure

Based on the serial CT images, the 3D microstructure was established with the help of the commercial software Avizo (version 9.3.0) developed by the FEI Company in France, which is widely used for 3D data visualization, analysis and modeling.

In the first step, the imported CT images were processed by a media filter to reduce noise and improve the quality (Figure 3a). Then, the 3D grayscale image was binarized to distinguish the pore space and solid phase by selecting a rational global threshold value (Figure 3b,c). It is noteworthy that some intra-aggregate pores with a size smaller than 1 μm are hard to observe clearly due to the resolution of CT images; therefore, these pore spaces may not be effectively extracted. The rationality of the threshold value was evaluated by comparing the threshold-based porosity with the volume-based porosity listed in Table 1. A close result or a lower threshold-based porosity is desirable.

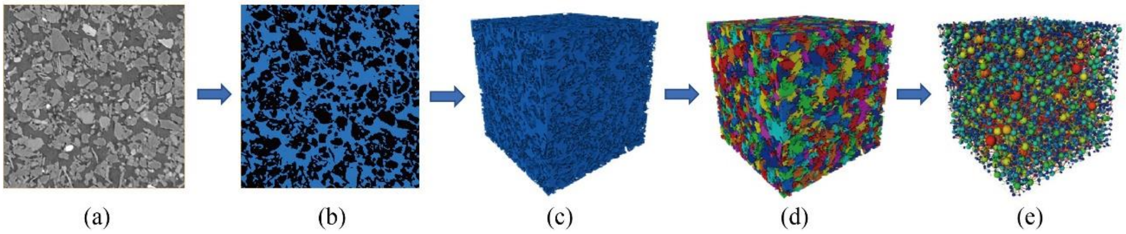

Figure 3. Process of 3D microstructure establishment: (**a**) CT image processed by media filter with a dimension of 600 × 600 μm^2, with the black area representing pores and the gray area representing particles; (**b**) binary image with the blue area representing pores in the loess; (**c**) 3D pore microstructure with a dimension of 600 × 600 × 570 μm^3; (**d**) pore separation with pores connected to each other; (**e**) pore network generation with the spheres representing true pores and the sticks between two spheres representing true throats.

The next step was to separate the connecting pores and contacted particles into individual ones for subsequent statistical analysis. The watershed algorithm has been widely used to obtain individual soil particles and pores [25]. Due to the various types of morphologies and mineral compositions, particle separation using the watershed algorithm required repeated adjustment and comparison with real particles in the grayscale image, and some operations such as "filling holes" before separation were also applied as required to avoid excessive separation. Some clay aggregates composed of clay and fine silts had to be treated as whole particles due to the limitation of the CT resolution. After separation, the particle arrangement, described as the maximum Feret diameter orientation, was extracted and analyzed because it greatly influences the structure stability and pore morphology within the loess. The orientation is defined as the angle φ between the maximum Feret diameter of the particles and the Z-axis ranging from 0 to 90°; a lower value indicates a more porous and unstable particle arrangement.

The pores in loess are only filled with gas, and the grayscale value is more intensive than that of soil particles. It is therefore much easier to separate pores using the watershed algorithm without further processing (Figure 3d). After segmentation, the pore size, expressed as the EqDiameter calculated for spheres with the same volume as an irregularly shaped pore body, can be obtained. Due to the limitation of the spatial resolution in CT scanning, some small pores with a size smaller than 1 μm or even several micrometers are hard to clearly observe. Therefore, pores smaller than 6 μm were not analyzed quantitatively in the following section.

The connectivity information can be obtained by generalizing the 3D pore structure as a pore network (Figure 3e). The spheres in the network represent the true pores with the same volume; the sticks represent throat connecting pores, with the cross-section size equal to the EqRadius (half of the EqDiameter) of the narrowest passage between two adjacent pores. The length of the sticks is defined as the distance between adjacent pore centers. In the network, the number of throats connecting to a sphere varying from zero to several is defined as the pore coordination number (CN), reflecting the pore connectivity; in general, a greater CN indicates better connectivity.

2.2.3. Range Determination of 3D Pore Structure

In this study, the scanning range was 1 mm both in diameter and height. It is inefficient to establish 3D structures at such a scale and extract the corresponding parameters. Therefore, it is necessary to select a representative elementary volume (REV) with a minimum size that is sufficient to reflect the pore structure correctly. Therefore, different volumes within the scanning range were selected to establish the 3D pore structures, and it was found that when the volume was more than 500 μm on each side, the porosity was close to that of the whole sample, and its variations became quite small. Therefore, the 3D pore structure was determined to be a cube with a dimension of $600 \times 600 \times 570$ μm^3.

3. Results and Discussion

3.1. Differences in Microstructure among the Studied Loess

Figure 4 presents the 2D CT images of the four groups of intact loess samples and the corresponding 3D microstructures, as well as the extracted statistical data. From the 2D CT images, it can be clearly observed that the LZ and HS loess have overall more homogeneous structures than the QY and JY loess. Angular and subangular silt and sand particles acting as skeleton particles connected primarily point to point dominate in the LZ and HS loess and form inter-particle pores. The particle arrangement in the former is much looser than that in the latter, which is favorable for collapse deformation and water seepage due to the considerable space and large free channels. The differences between the LZ and HS loess can also be visually observed by comparing the 3D microstructure after binarization and the 3D Euclidean distance map, as shown in Figure 4e,g, as well as Figure 4i,k. In the QY and JY loess, more clay and fine silt particles are observed to adhere to skeleton particles or mix with skeleton particles and form aggregates, and some aggregates are further cemented to form buttresses; therefore, in addition to inter-particle (aggregate) pores, intra-aggregate pores within aggregates and buttresses are widely observed. It can also be observed that there are some pores surrounded by smaller pore channels to form relatively closed spaces, named constricted pores, with sizes ranging from tens to even hundreds of microns, which can be clearly observed in the 3D Euclidean distance map in Figure 4j (QY loess) and Figure 4l (JY loess), different from the inter-particle pores forming free pore channels in Figure 4i (LZ loess) and Figure 4k (HS loess).

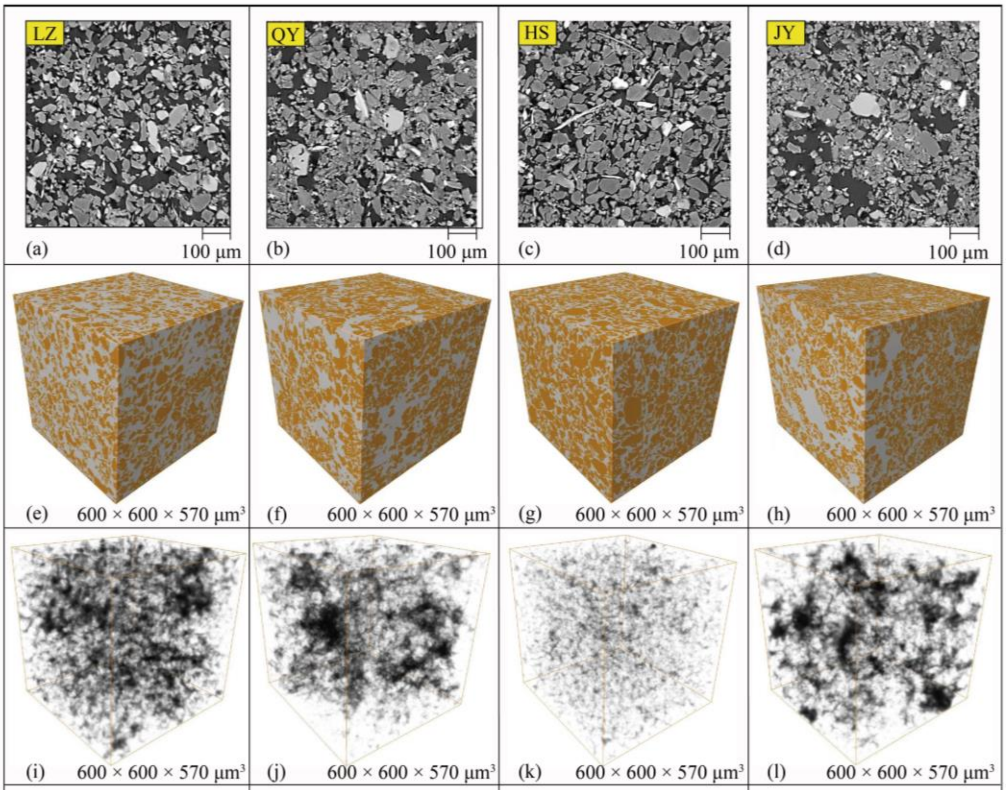

Total pore number: 9,158 Total CN: 72,895 Average CN: 7.95	Total pore number: 14,129 Total CN: 126,424 Average CN: 8.94	Total pore number: 10,895 Total CN: 83,367 Average CN: 7.65	Total pore number: 15,041 Total CN: 122,095 Average CN: 8.11

Figure 4. Comparison of the pore structures of the four loess samples: (**a**–**d**) CT images of the LZ, QY, HS and JY loess samples; (**e**–**h**) 3D microstructures with the gray volume representing the pore space and the yellow volume representing particles that have not been separated; (**i**–**l**) 3D Euclidean distance maps with each voxel representing the shortest distance from the voxel to the boundary between the pore space and solid particles, showing the pore microstructures of the four loess samples.

To better observe the differences in the pore structures of the four loess samples, the statistical data extracted from the corresponding 3D microstructures, including the total pore number, total CN and average CN, are also listed in the figure. The JY and QY loess have overall greater pore numbers than the HS loess and LZ loess, which can be primarily attributed to the particle size distribution and arrangement. The former two loess have more fine silt particles than the latter two loess. These particles fill in the inter-particle pores and separate them into smaller inter-particle pores. Accordingly, the total CNs are higher in the former two loess. The QY loess has the largest average CN, followed by the JY and LZ loess, while the HS loess has the lowest value, indicating it has the weakest connectivity among the pores. However, it should be noted that a higher CN is favorable for fluid seepage, while it does not indicate good permeability. The size of throats connecting pores may be a more significant factor influencing soil permeability.

To further explore and interpret the differences in pores within the four loess samples, the parameters related to the particle arrangement, pores, throats and connectivity were extracted from the above 3D microstructures and analyzed quantitatively.

3.2. Differences in Particle Arrangement among the Studied Loess

Figure 5 presents the orientation φ distributions of the four loess samples. The particles with φ in the range of 75–85° have an overall higher number percentage than those with φ ranging from 25 to 45°, indicating that more particles with the maximum Feret diameter are distributed in the direction close to the horizontal instead of the vertical plane. In particular, the gap in the HS loess is much more apparent than that in the other three loess samples, suggesting a more stable particle arrangement, which partially explains its denser pore structure shown in Figure 4.

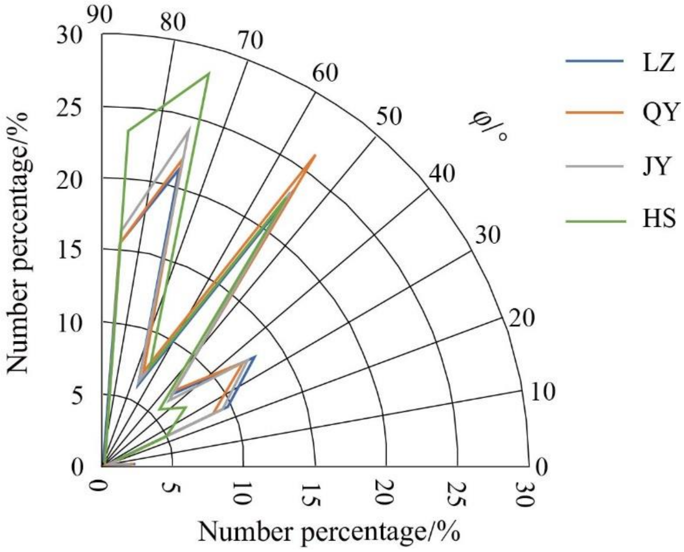

Figure 5. Number percentages of the particle orientation of the four loess samples.

3.3. Differences in Pore Parameters among the Studied Loess

Figure 6 presents the pore volume percentage distributions of the four loess samples, which are similar to a normal distribution, as shown in Expression (1), where the parameters μ (μ_p for pores and μ_t for throats) and σ (σ_p for pores and σ_t for throats) reflect the mean value and decentralization degree of the normal curve. The parameters of the fitting curves are listed in Table 3. The LZ loess has the largest μ_p, followed by the JY loess, QY loess and HS loess, indicating that the pores contributing to the major pore space are generally larger than those of the other three loess samples. The HS loess has a much smaller σ_p compared with the other three loess samples, suggesting a much more concentrated distribution of the pore volume.

$$f(x) = \frac{1}{\sqrt{2\pi}\sigma} e^{-\frac{(x-\mu)^2}{2\sigma^2}} \tag{1}$$

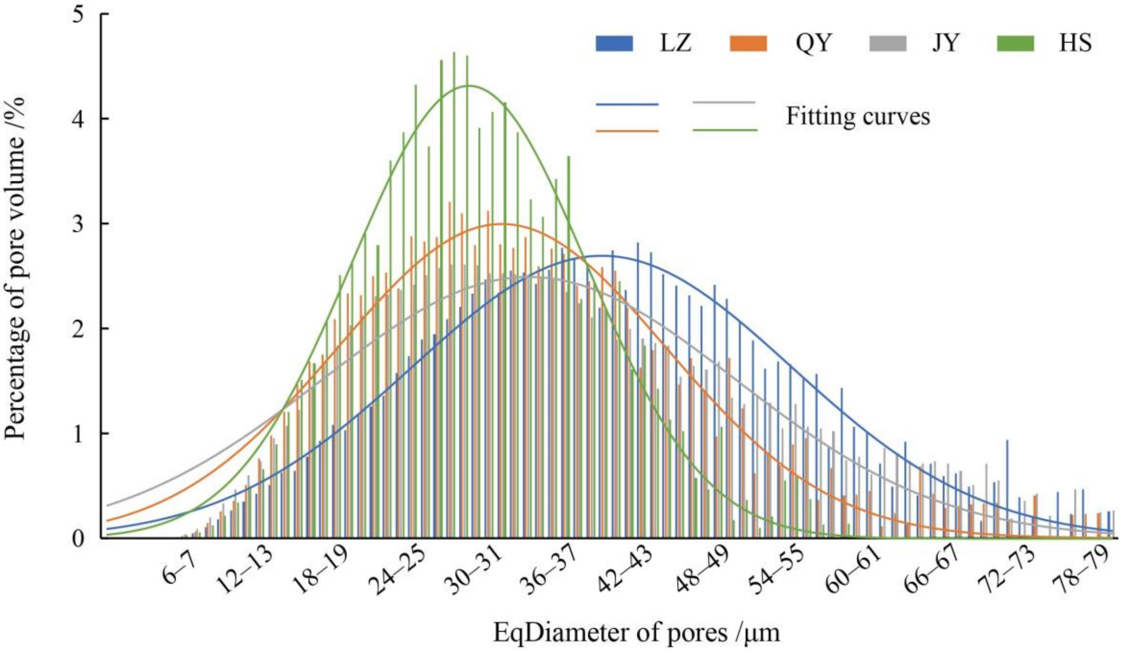

Figure 6. Pore size distributions of the four loess samples.

Table 3. Parameters of the fitting curves for the pore size distribution.

Samples	**Pore Size Distribution (Normal Curve)**		
	μ_p	σ_p	R^2
LZ	39.89	14.92	0.967
QY	32.03	12.91	0.9488
JY	34.16	16.28	0.9282
HS	29.44	9.25	0.9635

Combined with the data in Figure 4, it can be found that the LZ loess has a smaller number of pores than the JY and QY loess, but a larger mean pore size. The HS loess is disadvantaged both in pore number and mean pore size compared with the other three loess samples. In the JY loess, the intra-aggregate pores smaller than a few microns that are difficult to recognize and extract from the CT images contribute to its high void ratio, while for the QY loess, although its pore number is as high as that of the JY loess, the void ratio is much smaller due to its small mean pore size. The differences in pore parameters among the four loess samples are basically in accordance with the CT observations in Figure 4 and greatly influence their collapse potential and water seepage.

3.4. Differences in Throat Parameters among the Studied Loess

Figures 7 and 8 describe the throat number percentages in the different throat EqRadius and length ranges of the four loess samples. All the throat size distributions are similar to a Gamma distribution, as shown in Expression (2), in which the parameters α and β reflect the decentralization degree and amplitude of the Gamma curve. Overall, more than 50% percent of the pores are mainly connected by throats with a size between 2 and 5 μm. The parameters of the fitting curves are listed in Table 4. The LZ loess has a larger α compared with the other three loess samples, indicating a more decentralized throat size distribution, with the highest proportion of throats larger than 6 μm, followed by the JY loess. The QY and HS loess show a similar distribution with the lowest proportion. The throat length distributions of the four loess samples are similar to a normal distribution. The LZ loess has the largest mean throat length with μ_t of 37.11, followed by the HS loess, QY loess and JY loess (Table 4). The length differences among the four loess samples are generally consistent with the CT observations in Figure 4, in which the pores in the LZ loess are featured by free and curved channels connected by a narrow throat; two adjacent channels are equivalent to two spheres with centers located far from each other, forming a relatively long throat. Meanwhile, for the JY and QY loess, some skeleton particles and fine silts or clays are bonded to each other and form sphere-like pores; the centers of adjacent pores are close to each other, resulting in a relatively short mean throat length.

$$f(x) = \frac{\beta^a}{\Gamma(a)} x^{a-1} e^{-\beta x},\ \Gamma(a) = \int_0^\infty t^{a-1} e^{-t} dt \tag{2}$$

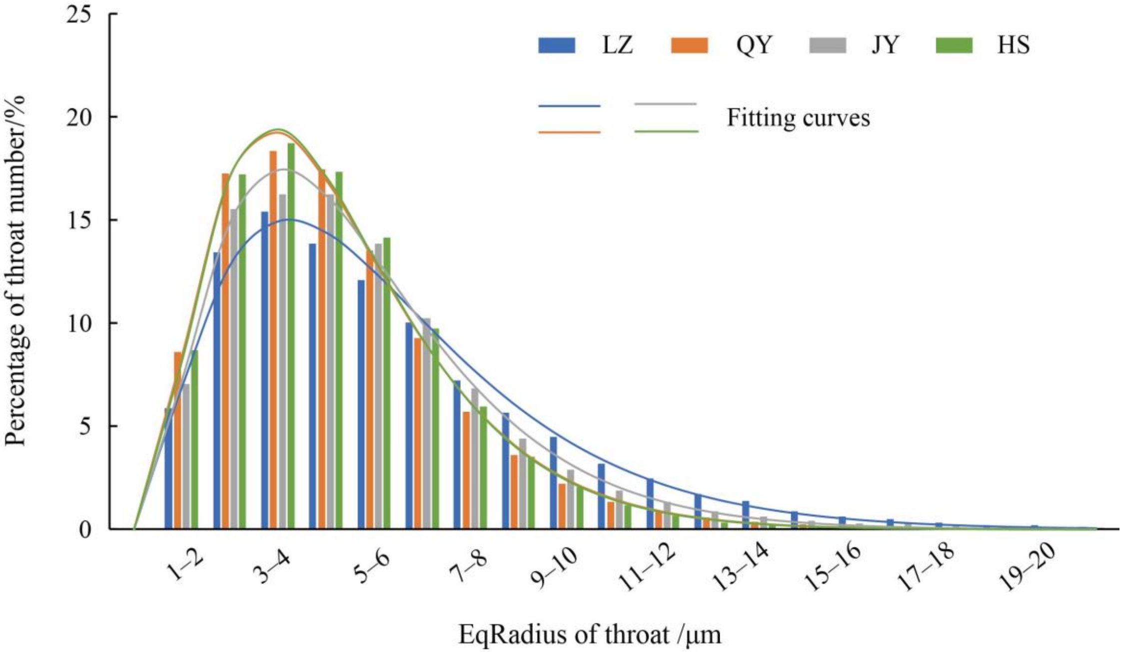

Figure 7. Throat size distributions of the four loess samples.

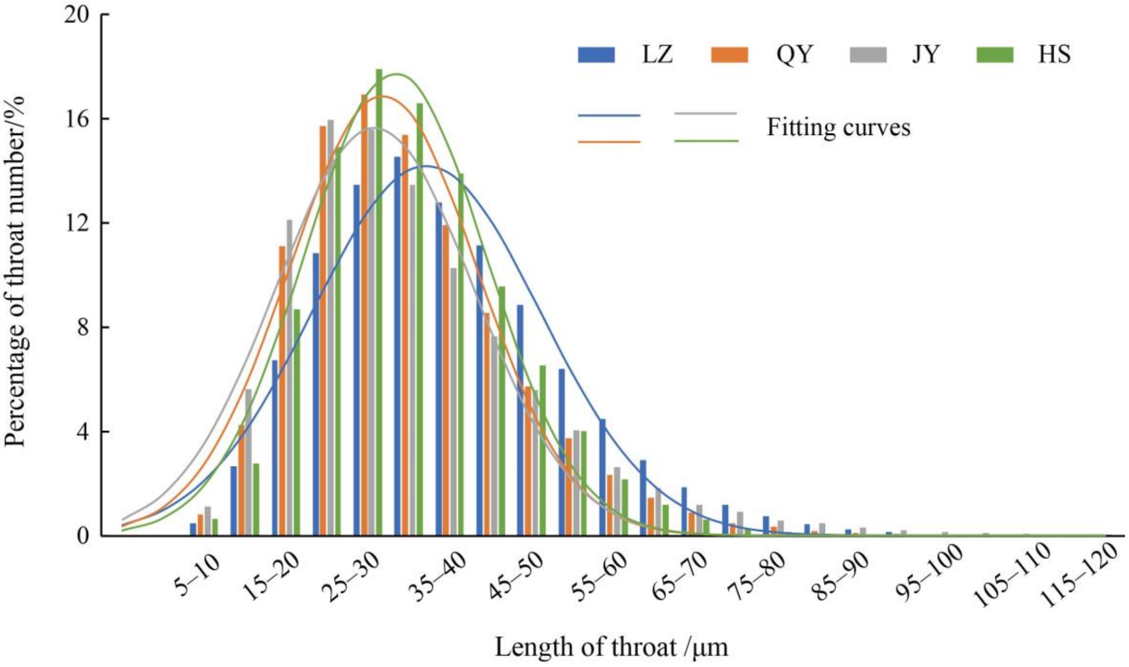

Figure 8. Throat length distributions of the four loess samples.

Table 4. Parameters of the fitting curves for the throat size and length distribution.

Samples	Throat Size Distribution (Gamma Curve)			Throat Length Distribution (Normal Curve)		
	α	β	R^2	μ_t	σ_t	R^2
LZ	1.989	2.617	0.9956	37.11	13.895	0.983
QY	1.382	3.068	0.9983	31.85	11.469	0.9731
JY	1.568	2.959	0.9971	30.82	12.077	0.9881
HS	1.352	3.133	0.9970	33.31	11.080	0.9765

The relationship between the pore and throat size of the four loess samples is plotted in Figure 9, in which the data were selected from all the throat data in one loess sample with an even interval for clear observation and comparison. The point in the figure represents the size of the throat and the average size of the two corresponding connected pores. The data are all located above the 1:1 line, data located in the upper left represent large pores connected by small throats, for example, in the JY, QY and LZ loess, there are some pores larger than 20 μm while connected by throats with a size of no more than one-sixth of the pore size, which may correspond to the constricted pores or spaced pores shown in Figure 4. These pores are actually not beneficial for water seepage in loess.

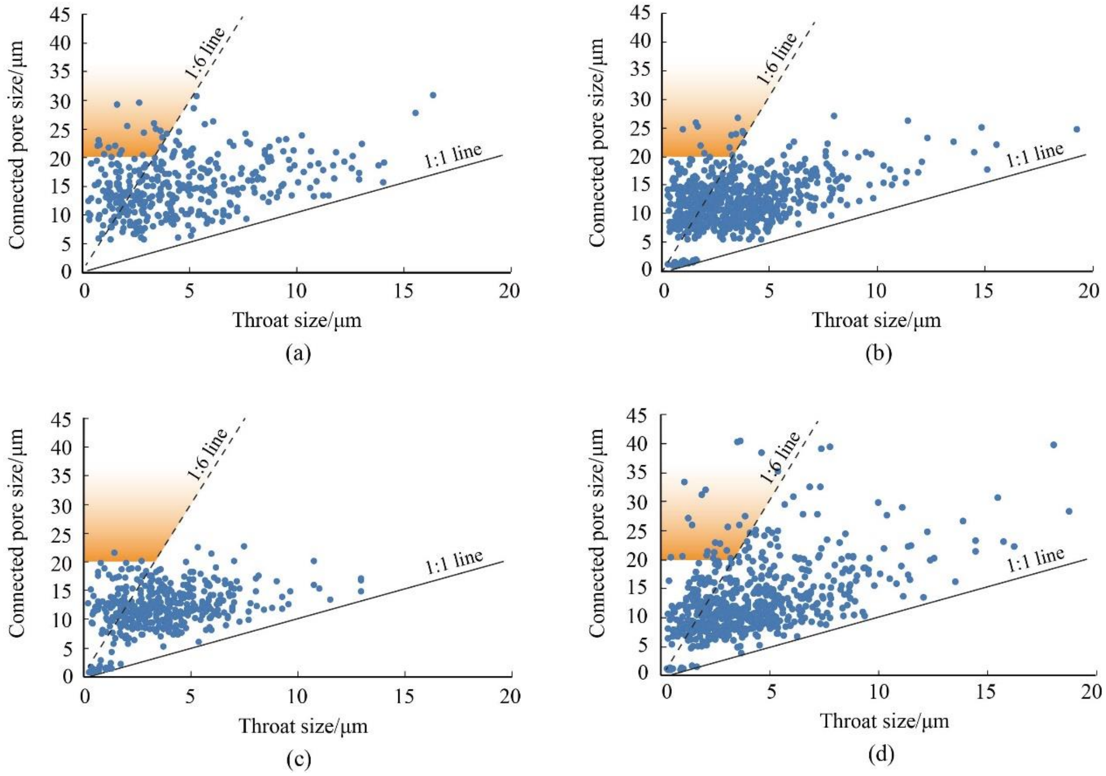

(a) (b) (c) (d)

Figure 9. Relationship between the throat size and the size of two connected pores: (**a**) LZ loess, (**b**) QY loess, (**c**) HS loess and (**d**) JY loess. The blue dots located in the bright red areas are the pores larger than 20 μm while connected by throats with a size of no more than one-sixth of the pore size.

3.5. Relationship between Hydraulic and Mechanical Behavior and Pore Structure

3.5.1. Collapsibility and Pore Structure

The pores within the loess are closely related to the loess collapse potential because they provide space for collapsible deformation. The collapsibility of the four loess samples was determined using a double-oedometer collapse test. The relationships between the coefficient of collapsibility and pore structure, including the void ratio and μ_p describing the pore size distribution, are plotted in Figure 10a,b, with partial data from related references [32]. It can be found that a high void ratio does not correspond to a large collapsibility coefficient. Taking the LZ and JY loess as an example, the JY loess has a void ratio of 1.21, larger than that of the LZ loess, while its collapsibility coefficient is less than half that of the LZ loess at 200 kPa. In addition, when loess have similar void ratios, this does not indicate a similar collapse potential, as illustrated by the data in the dotted circle. The pore size distribution, instead of the void ratio, seems to play a more important role in the collapse potential. In Figure 10b, a strong correlation between the collapsibility coefficient and μ_p is observed, the collapsibility coefficient at 200 kPa increases with the increase in μ_p. Therefore, loess collapsibility is closely related to the size of pores contributing to the major pore space. Notably, the void ratio is undoubtedly the precondition for loess collapse, although it shows weak relevance to collapsibility. In addition, the pore size distribution is not the only factor influencing loess collapse; the mineral composition and bonding materials and types may contribute to the strength of loess and play an important role in collapse deformation.

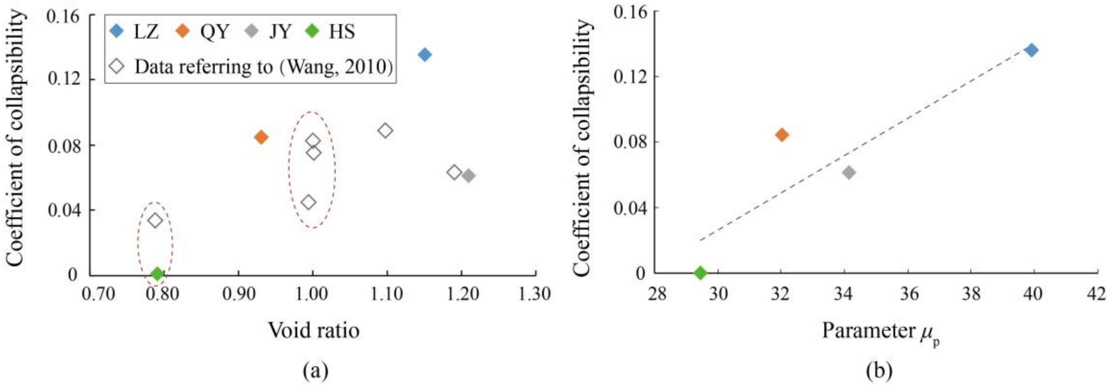

(a) (b)

Figure 10. Relationships between the coefficient of collapsibility and the (**a**) void ratio [32] and (**b**) μ_p.

3.5.2. Permeability and Pore Structure

The pores within loess have a considerable effect on its permeability because they provide channels for water seepage [9,16,33]. The relationships between permeability and pore structure, including the void ratio, average CN, μ_t describing the throat length and a describing the throat size, are plotted in Figure 11a–d, respectively. The data in the figure primarily came from related references [23,28,34–37]. It is noteworthy that compared with the throat size and length, the void ratio shows a weak correlation with loess permeability, loess with small void ratio does not correspond to weak permeability. For example, the HS loess has the lowest void ratio of 0.79, while the corresponding permeability is about twice as high as that of the JY loess with a large void ratio of 1.21. A large CN is favorable for water seepage, but it does not indicate a good permeability, as illustrated in Figure 11b. The throat length (Figure 11c) and size (Figure 11d) within loess show stronger positive correlations with permeability. The LZ and HS loess have a channel-like pore structure with a larger throat length than the JY and QY loess with more sphere-like pores, which allows desirable seepage channels and good permeability. The throat size also greatly influences loess permeability, which has been illustrated in some studies, while according to Figure 11d, it can be found that the JY loess has a larger a than the HS loess, indicating a higher proportion of large throats; while its permeability is slightly weaker than that of the HS loess, this is mainly limited by the small pores within the JY loess. The JY loess has more aggregates or buttress forming intra-aggregate pores than the LZ and HS loess, which limits its water seepage, although it has an overall larger throat size for inter-particle pores. Therefore, loess permeability is closely related to the whole pore structure and channel-like pore structures, as observed in the LZ and HS loess, are more desirable for water seepage; meanwhile, small pores in loess play a crucial role in limiting its water seepage.

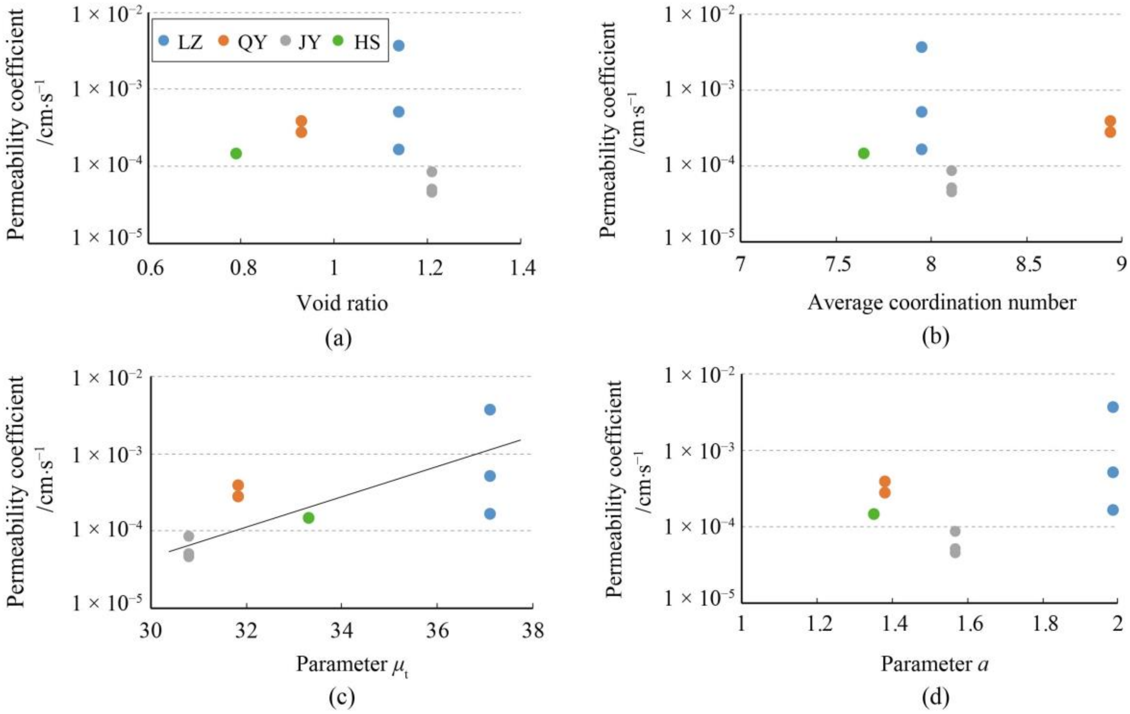

(a) (b) (c) (d)

Figure 11. Relationships between the coefficient of collapsibility and the (**a**) void ratio, (**b**) average pore number, (**c**) μ_t and (**d**) a.

3.6. Future Research

The pore structures of the four loess samples reported in this paper were fully investigated via 3D qualitative and quantitative characterization, and the correlations between the pore structures and hydraulic and mechanical behaviors of the loess were confirmed. When loess is subjected to environmental conditions of loading, wetting or freezing and thawing, the pore structure shows various changing features among different samples correspondingly. Research on these variations at the microscale can help to investigate and explore the process and mechanism of these hydraulic and mechanical behaviors. Notably, the pore structure within loess is primarily determined by the particle composition and arrangement as well as the mineral components. The mineral components greatly influence the bonding strength, particularly under environmental conditions, and, therefore, further cause the pore structure to change. Therefore, the mineral components in loess and their chemical reactions under environmental conditions deserve to be paid more attention to in future research. Moreover, much smaller scale characterization (for example, intra-aggregate pores) is limited when using μ-CT technology; thus, further research is required to combine μ-CT and Focus Ion Beam (FIB) for the multi-scale characterization of loess microstructure.

4. Conclusions

The 3D microstructures of Malan loess from Lanzhou, Qingyang, Hengshan and Jingyang were established based on μ-CT scanning. The corresponding microstructural parameters were compared and analyzed quantitatively, and their influences on loess permeability and collapsibility were investigated to interpret the intrinsic mechanism of the macro behaviors. The main outcomes of this study are summarized as follows.

(1) The LZ and HS loess both show overall homogeneous structures, with a more porous arrangement in the former. Angular and subangular silt and sand particles connected primarily point to point dominate in the LZ and HS loess and form inter-particle pores. The QY and JY loess have more clay and fine silt particles mixing with skeleton particles that form aggregates or buttresses, and more intra-aggregate pores within aggregates and buttresses and constricted pores are observed in these two loess samples.

(2) The pore size distributions of the four loess samples are similar to a normal distribution, and their throat size distributions are similar to a gamma distribution. The HS loess shows a more concentrated pore size distribution compared with the other three loess samples. Overall, the LZ loess has the largest pore size, followed by the JY loess, QY loess and HS loess, which is consistent with the throat sizes of the four loess samples. The average CNs of the LZ and HS loess are 7.95 and 7.65, lower than those of the QY and JY loess with average CNs of 8.94 and 8.11, while the throat lengths in the former two loess are larger than those in the latter two loess.

(3) The void ratio is undoubtedly the precondition for loess collapse, but it shows a weak relationship with collapsibility. The size of pores contributing to the major pore space presents a positive correlation with loess collapsibility. The throat length is more closely related to loess permeability than the void ratio, average CN and throat size, as a large throat length indicates a channel-like pore structure, which is favorable for water seepage; large throats are also desirable for water seepage, while the existence of small pores limits water seepage and determines the permeability directly.

Author Contributions: Conceptualization, review and editing, Y.N.; data process and analysis and writing—original draft, Y.-N.W.; methodology and laboratory tests, K.L.; investigation and field sampling, Y.C. All authors have read and agreed to the published version of the manuscript.

Funding: This research was funded by the National Natural Science Foundation of China (Grant Number. 42002285), and the Key R&D Program of Shaanxi Province (Grant Number. 2023-YBNY-234).

Data Availability Statement: The data that support the findings of this study are available from the corresponding author upon reasonable request.

Conflicts of Interest: The authors declare no conflict of interest.

References

1. Smalley, I.; O'Hara-Dhand, K.; Kwong, J. China: Materials for a Loess Landscape. *Catena* **2014**, *117*, 100–107. [CrossRef]
2. Li, Z.X.; Wang, J.D.; Yang, S.; Liu, S.H.; Li, Y.W. Characteristics of Microstructural Changes of Malan Loess in Yan'an Area during Creep Test. *Water* **2022**, *14*, 438. [CrossRef]
3. Peng, J.B.; Wang, S.K.; Wang, Q.Y.; Zhuang, J.Q.; Huang, W.L.; Zhu, X.H.; Leng, Y.Q.; Ma, P.H. Distribution and Genetic Types of Loess Landslide in China. *J. Asian Earth Sci.* **2019**, *170*, 329–350. [CrossRef]
4. Zhuang, J.Q.; Peng, J.B.; Wang, G.H.; Javed, L.; Wang, Y.; Li, W. Distribution and Characteristics of Landslide in Loess Plateau: A Case Study in Shaanxi Province. *Eng. Geol.* **2018**, *236*, 89–96. [CrossRef]
5. Huang, Y.H.; Feng, W.; Li, Z.G. Characteristics and Geological Disaster Mode of the Rainstorm Happened on July 3rd 2013 in Yanan Area of Shaanxi Province. *J. Catastrophol.* **2014**, *29*, 54–59. (In Chinese)
6. Gao, G.R. Classification of microstructures of loess in China and their collapsibility. *Sci. Sin.* **1981**, *7*, 962–970.
7. Liu, Z.; Liu, F.Y.; Ma, F.L.; Wang, M.; Bai, X.H.; Zheng, Y.L.; Yin, H.; Zhang, G.P. Collapsibility, Composition, and Microstructure of Loess in China. *Can. Geotech. J.* **2016**, *53*, 673–686. [CrossRef]
8. Ge, M.M.; Pineda, J.A.; Sheng, D.C.; Burton, G.J.; Li, N. Microstructural Effects on the Wetting-induced Collapse in Compacted Loess. *Comput. Geotech.* **2021**, *138*, 104359. [CrossRef]
9. Xu, P.P.; Zhang, Q.Y.; Qian, H.; Qu, W.G.; Li, M.N. Microstructure and Permeability Evolution of Remolded Loess with Different Dry Densities under Saturated Seepage. *Eng. Geol.* **2021**, *282*, 105875.
10. Ng, C.W.W.; Sadeghi, H.; Jafarzadeh, F.; Sadeghi, M.; Zhou, C.; Baghbanrezvan, S. Effect of Microstructure on Shear Strength and Dilatancy of Unsaturated Loess at High Suctions. *Can. Geotech. J.* **2020**, *57*, 221–235. [CrossRef]
11. Assallay, A.M.; Rogers, C.D.F.; Smalley, I.J. Formation and Collapse of Metastable Particle Packings and Open Structures in Loess Deposits. *Eng. Geol.* **1997**, *48*, 101–115. [CrossRef]
12. Wang, L.; Li, X.A.; Li, L.C.; Hong, B.; Yao, W.; Lei, H.N.; Zhang, C. Characterization of the collapsible mechanisms of Malan loess on the Chinese Loess Plateau and their effects on eroded loess landforms. *Hum. Ecol. Risk Assess.* **2020**, *26*, 2541–2566. [CrossRef]
13. Deng, L.S.; Fan, W.; Chang, Y.P.; Yu, B.; Wei, Y.N.; Wei, T.T. Microstructure Quantification, Characterization, and Regional Variation in the Ma Lan Loess on the Loess Plateau in China. *Int. J. Geomech.* **2021**, *21*, 04021143. [CrossRef]
14. Xiao, T.; Li, P.; Pan, Z.H.; Hou, Y.F.; Wang, J.D. Relationship between Water Retention Capacity and Pore-size Distribution of Compacted Loess. *J. Soil. Sediment.* **2022**, *22*, 3151–3165. [CrossRef]
15. Muñoz-Castelblanco, J.A.; Pereira, J.M.; Delage, P.; Cui, Y.J. The Water Retention Properties of A Natural Unsaturated Loess from Northern France. *Géotechnique* **2012**, *62*, 95–106. [CrossRef]
16. Xu, P.P.; Zhang, Q.Y.; Qian, H.; Li, M.N.; Yang, F.X. An Investigation into the Relationship between Saturated Permeability and Microstructure of Remolded Loess: A Case Study from Chinese Loess Plateau. *Geoderma* **2021**, *382*, 114774. [CrossRef]

17. Li, T.L.; Zhang, H.; Li, P.; Kang, H.W.; Ge, S.L. Mode Analysis of Pore Distribution and Soil-Water Characteristic Curve of Malan Loess under Different Depositional Environments. *Hydrogeol. Eng. Geol.* **2020**, *47*, 107–114. (In Chinese)
18. Barden, L.; Mcgown, A.; Collins, K. The Collapse Mechanism in Partly Saturated Soil. *Eng. Geol.* **1973**, *7*, 49–60. [CrossRef]
19. Wei, Y.N.; Fan, W.; Yu, B.; Deng, L.S.; Wei, T.T. Characterization and Evolution of Three-dimensional Microstructure of Malan Loess. *Catena* **2020**, *192*, 104585. [CrossRef]
20. Yu, B.; Fan, W.; Dijkstra, T.A.; Wei, Y.N.; Deng, L.S. Heterogeneous Evolution of Pore Structure During Loess Collapse: Insights from X-ray Micro-computed Tomography. *Catena* **2021**, *201*, 105206. [CrossRef]
21. Lei, X.Y. Characteristics of Loess Pore Distribution in North Shaanxi and East Gansu. *Chin. Sci. Bull.* **1985**, *30*, 656–661.
22. Gao, G.R. Formation and Development of the Structure of Collapsing Loess in China. *Eng. Geol.* **1988**, *25*, 235–245.
23. Wei, T.T.; Fan, W.; Yuan, W.N.; Wei, Y.N.; Yu, B. Three-dimensional Pore Network Characterization of Loess and Paleosol Stratigraphy from South Jingyang Plateau, China. *Environ. Earth Sci.* **2019**, *78*, 333. [CrossRef]
24. Wang, J.D.; Li, P.; Ma, Y.; Vanapalli, S.; Wang, X.G. Change in Pore-size Distribution of Collapsible Loess due to Loading and Inundating. *Acta Geotech.* **2020**, *15*, 1081–1094. [CrossRef]
25. Yuan, W.N.; Fan, W. Quantitative study on the microstructure of loess soils at micrometer scale via X-ray computed tomography. *Powder Technol.* **2022**, *408*, 117712. [CrossRef]
26. Li, Y.R.; He, S.D.; Deng, X.H.; Xu, Y.X. Characterization of Macropore Structure of Malan Loess in NW China Based on 3D Pipe Models Constructed by Using Computed Tomography Technology. *J. Asian Earth Sci.* **2018**, *154*, 271–279. [CrossRef]
27. Qiao, J.B.; Liu, X.T.; Zhu, Y.J.; Jia, X.X.; Shao, M.A. Three-dimensional quantification of soil pore structure in wind-deposited loess under different vegetation types using industrial X-ray computed tomography. *Catena* **2021**, *199*, 105098. [CrossRef]
28. Wei, Y.N.; Fan, W.; Yu, N.Y.; Deng, L.S.; Wei, T.T. Permeability of Loess from the South Jingyang Plateau under Different Consolidation Pressures in terms of the Three-dimensional Microstructure. *Bull. Eng. Geol. Environ.* **2020**, *79*, 4841–4857. [CrossRef]
29. Xu, J.; Li, Y.F.; Ren, C.; Wang, S.H.; Vanapalli, S.K.; Chen, G.X. Influence of Freeze-thaw Cycles on Microstructure and Hydraulic Conductivity of Saline Intact Loess. *Cold Reg. Sci. Technol.* **2021**, *181*, 103183. [CrossRef]
30. Lin, Z.G.; Liang, W.M. Engineering Properties and Zoning of Loess and Loess-like Soils in China. *Can. Geotech. J.* **1982**, *19*, 76–91. [CrossRef]
31. Ministry of Water Resources of the People's Republic of China. *Specification of Soil Test*; SL 237-1999; China Water Resources and Hydropower Press: Beijing, China, 1999. (In Chinese)
32. Wang, M. Study on Structure of Collapsible Loess in China. Ph.D. Thesis, Taiyuan University of Technology, Taiyuan, China, 2010. (In Chinese).
33. Shao, T.J.; Wang, R.J.; Xu, Z.P.; Wei, P.R.; Zhao, J.B.; Niu, J.J.; Song, D.X. Permeability and Groundwater Enrichment Characteristics of the Loess-Paleosol Sequence in the Southern Chinese Loess Plateau. *Water* **2020**, *12*, 870. [CrossRef]
34. Yue, F.; Ren, X.; Wang, X.L.; Tian, W.T. Experimental Study on the Influence of Soil Structure Index on Loess Permeability. *Adv. Mater. Sci. Eng.* **2022**, *2022*, 9618732. [CrossRef]
35. Xiao, D.H.; Feng, W.J.; Zhang, Z.; Ming, J.; Wang, Q. Research on the Lanzhou Loess's Permeabilities Changing with Freezing-thawing Cycles. *J. Glaciol. Geocryol.* **2014**, *36*, 1192–1198. (In Chinese)
36. Yuan, Z.X.; Sha, H.; Zhu, Y.P.; Shi, Y.C.; Zhao, W.C. Experimental Study on the Permeability of Compacted Loess. *Geotech. Investig. Surv.* **2019**, *47*, 1–7. (In Chinese)
37. Yang, F.X. Experimental Study on Permeability and Microstructure Characteristics of Malan Loess. Master's Thesis, Chang'an University, Xi'an, China, 2021. (In Chinese).